Nanoscale

PAPER

View Article Online
View Journal | View Issue

Cite this: *Nanoscale*, 2021, **13**, 14119

Surface properties modulate protein corona formation and determine cellular uptake and cytotoxicity of silver nanoparticles†

Marianna Barbalinardo, [a] Jessika Bertacchini,[b] Linda Bergamini,[c] Maria Sara Magarò, [b] Luca Ortolani,[d] Alessandra Sanson,[c] Carla Palumbo,[b] Massimiliano Cavallini [a] and Denis Gentili *[a]

Nanoparticles (NPs) have been studied for biomedical applications, ranging from prevention, diagnosis and treatment of diseases. However, the lack of the basic understanding of how NPs interact with the biological environment has severely limited their delivery efficiency to the target tissue and clinical translation. Here, we show the effective regulation of the surface properties of NPs, by controlling the surface ligand density, and their effect on serum protein adsorption, cellular uptake and cytotoxicity. The surface properties of NPs are tuned through the controlled replacement of native ligands, which favor protein adsorption, with ligands capable of increasing protein adsorption resistance. The extent and composition of the protein layer adsorbed on NPs are strongly correlated to the degree of ligands replaced on their surface and, while BSA is the most abundant protein detected, ApoE is the one whose amount is most affected by surface properties. On increasing the protein resistance, cellular uptake and cytotoxicity in mouse embryonic fibroblasts of NPs are drastically reduced, but the surface coating has no effect on the process by which NPs mainly induce cell death. Overall, this study reveals that the tuning of the surface properties of NPs allows us to regulate their biological outcomes by controlling their ability to adsorb serum proteins.

Received 19th November 2020,
Accepted 19th July 2021

DOI: 10.1039/d0nr08259g

rsc.li/nanoscale

Introduction

Over the past decades, nanoparticles (NPs) have been extensively studied for biomedical applications, ranging from prevention, early diagnosis and treatment of diseases as their unique and highly tunable physical, chemical, and biological properties promise to overcome some critical shortcomings of conventional medicine, such as poor bioavailability and low target specificity, as well as facing the challenges related to improving the quality of life of patients during treatments. However, the lack of the basic understanding of how NPs interact with the biological environment and, in turn, with living systems has severely limited their potential in medicine.[1–6] Although significant progress has been made to overcome some critical limits, to date, independently of material (organic or inorganic) and targeting strategy (active or passive), the delivery of NPs to the target tissue is less than 1% of the injected dose and their clinical translation has been limited. Although NPs can be engineered with precise functional properties for specific and nonspecific cellular targeting, they have to face physical and biological barriers before reaching the target tissue, resulting in a very low nanoparticle delivery efficiency.[7,8] There is no simple correlation between biological responses and synthetic identity of NPs (*i.e.*, size, shape and surface properties post-synthesis) as, in biological fluids, their physicochemical properties can drastically change following the interactions and adsorption onto the surface of extracellular proteins and other biological molecules, creating the so-called protein corona. The structure and composition of the protein corona, which depend on the combination of synthetic identity of NPs with the nature of the biological fluid and exposure time, can be sufficiently long lived to determine the biological identity of NPs and, therefore, can critically regulate their physiological responses.[5,9–11] Thus, elucidating the role

[a]*Consiglio Nazionale delle Ricerche, Istituto per lo Studio dei Materiali Nanostrutturati (CNR-ISMN), via P. Gobetti 101, 40129 Bologna, Italy. E-mail: denis.gentili@cnr.it*
[b]*Department of Biomedical, Metabolic and Neural Sciences, Section of Human Morphology, University of Modena and Reggio Emilia, Via del Pozzo 71, 41124 Modena, Italy*
[c]*Consiglio Nazionale delle Ricerche, Istituto di Scienza e Tecnologia dei Materiali Ceramici (CNR-ISTEC), via Granarolo 64, 48018 Faenza, Italy*
[d]*Consiglio Nazionale delle Ricerche, Istituto per la Microelettronica e Microsistemi (CNR-IMM), via P. Gobetti 101, 40129 Bologna, Italy*
†Electronic supplementary information (ESI) available. See DOI: 10.1039/d0nr08259g

of each physicochemical parameter of NPs is needed to control their identity in biological media and, in turn, to develop effective strategies to design long-circulating and target-specific NPs with increased delivery efficiency and improved therapeutic response.[12–16] Among all physicochemical parameters that affect the nature and amount of protein adsorption, the surface properties of NPs have been reported to play the most significant role in the formation of the protein corona.[17,18] Silver nanoparticles (AgNPs) have been extensively studied for biomedical applications and, because of their antibacterial and antifungal properties, they are one of the most diffuse nanomaterials in customer products.[1,19] We have recently demonstrated that surface coating of AgNPs strongly affects the adsorption of serum proteins and, in turn, their cellular uptake and cytotoxicity in mouse embryonic fibroblasts. In particular, citrate-coated AgNPs are promptly coated and stabilized by a protein corona and show a time- and dose-dependent toxicity, while the passivation of the NP surface with an oligo(ethylene glycol) (OEG)-terminated alkanethiol drastically reduces both the adsorption of proteins and the cytotoxicity.[20,21] However, the engineering of nanomaterials capable of overcoming biological barriers needs the basic understanding of how key design parameters of NPs affect the serum protein adsorption and the resulting biological outcomes.

In the present work, we report the effective gradual modulation of the surface properties of NPs, by controlling the surface ligand density, and their effect on serum protein adsorption, cellular uptake and cytotoxicity, aiming to provide further insight for the engineering of nanomaterials exploiting the manipulation of the protein corona. As schematically shown in Scheme 1, we use citrate-coated AgNPs and gradually modify their surface properties through the controlled displacement of citrate ions with an OEG-terminated alkanethiol, namely (11-mercaptoundecyl)hexa(ethylene glycol) (hereafter indiscriminately referred to as "EG_6OH" or "ligand", see Fig S1 in the ESI† for molecular structures). The gradual modification of the surface properties as well as the consequent modulation of the resistance to the protein adsorption of the AgNPs are studied by UV-vis spectroscopy, anion-exchange chromatography, and electrolyte-induced aggregation tests and by assessing the hydrodynamic diameter and zeta potential.

The increase of ligand density gradually increases the resistance to protein adsorption of the AgNPs, thus drastically affecting both the composition and amount of proteins that constitute their protein corona. These changes in the protein corona have, in turn, a significant impact on the biological identity of nanoparticles and, therefore, on their interactions with cells. We show that the uptake and cytotoxic activity of AgNPs on mouse embryonic fibroblasts strongly correlate with the surface properties, in fact, both proportionally decrease with the increasing ligand density, but the process by which AgNPs mainly induce cell death remains the same. These results reveal that the surface properties of NPs regulate their interactions with cells and, in turn, dictate their biological outcomes. The synergism between the surface coverage and biological identity of NPs can be exploited for their rational design and engineering, thus thoroughly tailoring their interactions with living systems to specific applications and minimizing the side effects.

Results and discussion

Alkanethiols terminated with an OEG unit have been extensively studied for their ability to form protein resistant self-assembled monolayers (SAMs) on gold and silver surfaces,[22–25] even when used in mixed SAMs.[26–28] The resistance to protein adsorption is determined by the internal and terminal hydrophilicity, the number of ethylene glycol units and lateral

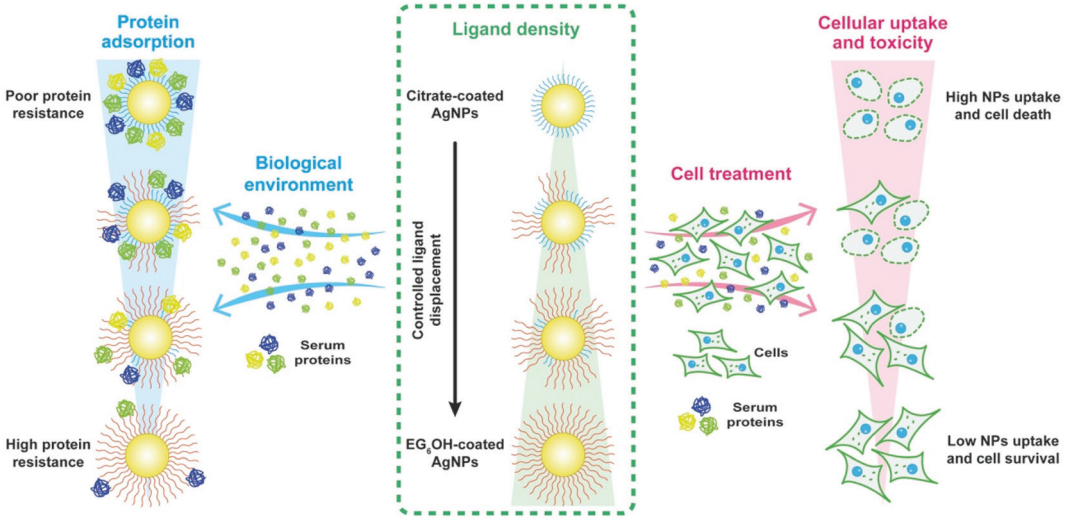

Scheme 1 Schematic illustration of the effect of ligand (EG_6OH) density on protein adsorption (left), cellular uptake and cytotoxicity (right) of AgNPs.

packing density of OEG-terminated alkanethiol used. The lateral packing density, which in turn determines the molecular conformation of the OEG moieties, can be affected both by the assembly solvent and the substrate material.[23,24] Among all, EG_6OH is an OEG-terminated alkanethiol capable of forming robust protein resistant SAMs on planar silver surfaces,[22,23] as well as on AgNPs,[20,21] regardless of the assembly solvent used.[24] Therefore, we have tuned the protein resistance properties of AgNPs through the controlled replacement of citrate ions, which favor surface protein adsorption,[20] with EG_6OH. Citrate-coated AgNPs having an average diameter of 22 ± 4 nm, as determined from transmission electron microscopy (TEM) analysis (Fig. 1a and b), were prepared as previously reported[29] and functionalized with increasing density of EG_6OH. Because thiol containing molecules bind strongly to the gold and silver surfaces and can displace other weakly bound ligands, such as citrate ions,[30] the density of the EG_6OH on the nanoparticle surface was controlled by varying the EG_6OH-to-nanoparticle ratio and quantified by a thiol depletion assay (see the Experimental section). The studied ligand densities range from AgNPs coated exclusively with citrate ions, *i.e.* NPs with EG_6OH density = 0 (hereafter indiscriminately referred to such NPs as "0" or "citrate-coated AgNPs"), to saturating density of EG_6OH (4.0 ± 0.1 EG_6OH per nm^2 – see the ESI†). Noteworthily, the saturation ligand density is in good agreement with values reported on planar surfaces[22] and gold nanoparticles.[31,32] Citrate-coated AgNPs show the characteristic localized surface plasmon resonance (LSPR) band centered at ~400 nm (S1a in the ESI†) that is red-shifted, without shape variation, upon surface functionalization with the ligand (Fig. 1c and a zoomed-in view of it in the ESI – Fig S1b†). We noticed the absence of the broadening of the LSPR band also for very low density (*i.e.* 0.6–0.8 EG_6OH per nm^2), thus revealing that there is no aggregation of AgNPs, contrary to what we previously reported for gold nanoparticles.[33] Fig. 1c inset shows the ligand density dependence of the plasmon band. Below the saturation density, the plasmon band maximum is found to red shift rapidly increasing the EG_6OH density, as a result of the gradual change of the refractive index of the surrounding environment.[34] On approaching saturation, the plasmon band maximum of AgNPs increases more slowly to reach its maximum value. Noteworthily, this trend is reproducible on all batches of citrate-coated AgNPs we have prepared and functionalized with EG_6OH (see for a different batch, ESI – Fig. S1c†).

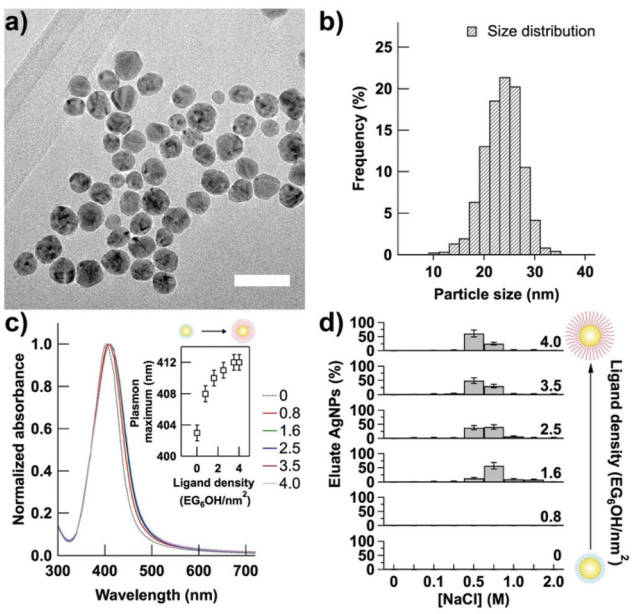

Fig. 1 (a) TEM image (scale bar: 50 nm) and (b) size distribution of citrate-coated AgNPs measured using ImageJ software by counting 1000 particles. (c) UV-Vis absorption spectra of AgNPs in sodium citrate (2 mM) as a function of EG_6OH density. Inset: dependence of the plasmon band maximum on the EG_6OH density. (d) Elution profile of AgNPs as a function of EG_6OH density on anion-exchange chromatography using increasing concentrations of NaCl.

The gradual replacement of citrate ions adsorbed on the nanoparticle surface with EG_6OH molecules was further confirmed by anion-exchange chromatography on diethylaminoethyl (DEAE) sepharose. Although AgNPs bind to the positively charged resin regardless of EG_6OH density, because they show a negative zeta potential (see below), their elution profile is drastically different as a function of surface coverage. As shown in Fig. 1d, AgNPs with low densities (≤0.8 EG_6OH per nm^2) bind irreversibly to the DEAE resin as they were not eluted even with a high concentration of NaCl (2 M). However, on increasing the ligand density, the elution of AgNPs takes place at lower concentrations of NaCl and almost complete elution of NPs was obtained with 0.5 M NaCl approaching the saturation density. The gradual increase of AgNP stability against irreversible adsorption onto resin is due to the replacement of weakly associated citrate ions on their surface, which can be easily displaced by the functional groups of the resin, with EG_6OH, in contrast, binding strongly to the nanoparticle surface. In addition, as we already reported for gold nanoparticles, the replacement of citrate ions with EG_6OH molecules leads to a decrease of electrostatic repulsions and a simultaneous increase of steric ones between the nanoparticles proportional to the extent of surface ligand substitution.[33] In agreement, the electrolyte-induced aggregation test showed that citrate-coated AgNPs are unstable at a salt concentration of 0.05 M, but the stability of NPs in saline solution increases following the increase of EG_6OH density to show good stability also in 1 M saline solution (the highest value tested) when the density reaches the saturation value (see ESI – Fig. S2†).

We have recently reported the key role of the adsorption of serum proteins onto the surface of AgNPs in mediating their cellular uptake and cytotoxic activity.[20] Therefore, to investigate the effect of EG_6OH density on serum protein adsorption, we measured the change of hydrodynamic diameter and zeta potential of the NPs after incubation in a growth medium containing fetal bovine serum (FBS) and subsequent extensive purification to remove unbound or weakly adsorbed proteins (see the Experimental section). As we already reported, the mean hydrodynamic diameter of citrate-coated AgNPs is

strongly increased by the incubation in serum-containing media. However, as shown in Fig. 2a, the discrepancy between the hydrodynamic diameter before and after incubation in the cellular medium becomes less significant increasing the density of EG_6OH and disappears, within the experimental error, when the saturation value is reached. As shown in Fig. 2b, the variation of zeta potential values before and after exposure to serum proteins shows a trend that is completely in agreement with what was observed with hydrodynamic diameters. Before incubation with serum proteins, the zeta potential of AgNPs becomes less negative with the increasing ligand density, as expected by the replacement of negatively charged citrate ions with EG_6OH molecules. Following the incubation with serum proteins and purification, the zeta potential values are lowered; however, this variation decreases as the EG_6OH density increases and it becomes insignificant when approaching the saturation density. Interestingly, the final value of zeta potential of AgNPs after incubation in the growth medium is almost the same regardless of the ligand density.

DLS and zeta potential data clearly show that the protein resistance of AgNPs is strictly correlated to their surface coverage, in fact the extent of protein adsorption on their surface increases with the increasing ligand density.

To further investigate the role of surface coverage, after incubation in a growth medium containing FBS and subsequent purification, serum proteins adsorbed on the surface of AgNPs were isolated and separated using polyacrylamide gel electrophoresis (PAGE) coupled with a protein stain (see the Experimental section). As shown in Fig. 2c, proteins separated from citrate-coated AgNPs (lane 3) showed several bands, marked by blue dashed squares and labeled 1–7, that were not present in the control (ctrl, lane 2), confirming their ability to adsorb a broad range of serum proteins. The proteins isolated from AgNPs functionalized with higher ligand density showed similar band patterns (Fig. 2c, lanes 4–9). However, the intensity of some bands decreases down to disappear with increasing ligand density, revealing that the composition of the serum protein layer adsorbed on the AgNPs is strongly dependent on the surface coverage. In agreement, semiquantitative densitometry analysis of PAGE lanes shows that the total amount of adsorbed proteins contained in the areas corresponding to bands 1–7 drastically decreases with the increasing EG_6OH density (blue circle, Fig. 2d); however, the adsorption of proteins was not completely eliminated even at the saturation density. Noteworthily, our results are in agreement with what was observed for the adsorption of a single protein on a planar gold surface functionalized either with a mixed layer of EG_6OH and n-alkanethiols[26,27] or with hydroxyl-terminated poly(ethylene glycol) (PEG)[36] and for the adsorption of serum proteins on gold nanoparticles functionalized with methoxy-terminated PEG.[37]

A more detailed investigation of the protein corona composition was performed using label-free liquid chromatography mass spectrometry (LC-MS/MS). Proteins separated in the

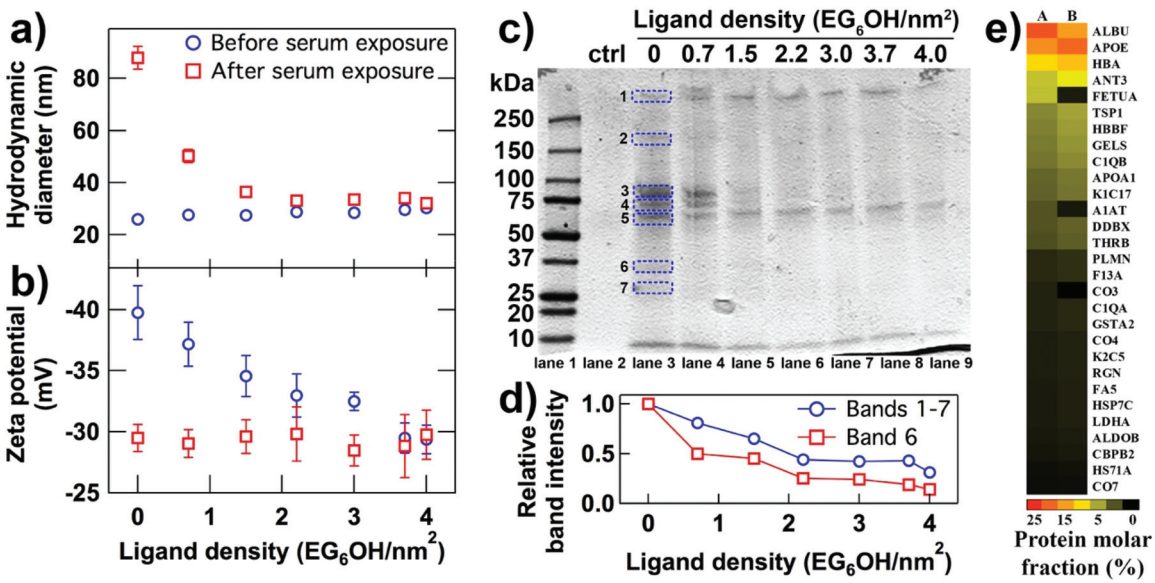

Fig. 2 (a) Hydrodynamic diameter and (b) zeta potential of AgNPs with different EG_6OH densities before (blue circle) and after (red square) incubation in growth media (exposure to serum proteins), and the values are summarized in Table S1 in the ESI.† (c) SDS-PAGE gel of adsorbed serum proteins on AgNPs with different EG_6OH densities. The molecular weight ladder is shown in lane 1. SDS-PAGE of products extracted from citrate-coated AgNPs not incubated in the growth medium was included as a control (ctrl, lane 2). (d) Densitometric analysis as a function of EG_6OH density of PAGE scan shown in Fig. 2c. Relative band intensity was calculated by measuring for each lane identical area corresponding to those marked by blue dashed squares only in lane 3 for convenience of clarity; (blue circle) sum of all (1–7) areas for each lane and (red square) only area 6. (e) Heat map of protein molar fractions identified and determined by proteomic mass spectrometry in the areas marked in lane 3 of Fig. 2c by blue dashed squares: sum of (A) 1–7 and (B) 2, 3, 4, 6 and 7 areas. Values were calculated from the emPAI of each protein identified by LC-MS/MS according to the equation: Protein content (mol %) = emPAI/$\sum$(emPAI).[35] Abbreviated protein names are explained in the ESI – Table S2.†

seven bands from citrate-coated AgNPs (lane 3, Fig. 2c) were excised, digested with trypsin and analyzed by LC-MS/MS. Protein molar fractions of serum proteins that constitute the corona of citrate-coated AgNPs are reported in Fig. 2e (column A) and summarized in Table S2 in the ESI.† A total of 29 serum proteins were identified in seven bands and their relative abundances were estimated quantitatively by calculating their exponentially modified protein abundance index (emPAI).[35] Overall, the most abundant protein detected in the corona is bovine serum albumin (BSA, 21% mol) followed by apolipoprotein E (ApoE, 16% mol), which is a protein involved in lipid transport and uptake.[38,39] Both the proteins were identified on different types of nanoparticles but, while the adsorption of albumin has been reported to protect nanomaterials from opsonization (dysopsonin effect), thus leading to an increase in their blood circulation times,[40–42] the adsorption of ApoE is reported to mediate the interaction of nanomaterials with low-density lipoprotein receptors (LDLR), promoting their uptake into endothelial cells[38,39] and hepatocytes.[43]

As mentioned above, the protein pattern changes with surface coverage, however, not all the bands (1–7 in Fig. 2c) show a significant decrease of intensity with increasing ligand density. As shown in Fig. 2c, bands 2, 3, 4, 6, and 7 show a marked decrease of the intensity upon the increase of ligand density, while bands 1 and 5 are not affected significantly, suggesting that not all proteins that constitute the corona of citrate-coated AgNPs are affected by replacement of citrate ions with EG_6OH molecules.

Therefore, for a deeper insight, we compared the relative protein abundance calculated considering the sum of all (1–7) bands *versus* the relative protein abundance calculated considering only bands whose intensity decreases more drastically with the increase of ligand density (*i.e.* bands 2, 3, 4, 6, and 7 in Fig. 2c). As schematically reported in Fig. 2e and summarized in Table S3 in the ESI,† while BSA is the most abundant protein that constitutes the corona (Fig. 2e, column A), ApoE is the most abundant protein when only PAGE bands whose intensity is clearly affected by the surface coverage are considered (Fig. 2e, column B), revealing that the content of ApoE in the corona is more affected by the ligand density than that of BSA. In addition, since ApoE was identified only in band 6, we compared the trend of the intensity of this band with the sum of all bands (1–7); as revealed by densitometric analysis, the amount of proteins in band 6 (red square, Fig. 2d) decreases more drastically with the increasing EG_6OH density than that of the sum of all bands (blue circle, Fig. 2d). Taking into account that ApoE represents almost the 60% mol of proteins contained in band 6 (see ESI – Table S4†), these results further confirm that the adsorption of ApoE, more than those of BSA, is influenced by the EG_6OH density.

To evaluate the impact of EG_6OH density on the interactions between the NPs and living systems, we performed studies of toxicity, based on 3-(4,5-dimethyl-2-thiazolyl)-2,5-diphenyltetrazolium bromide (MTT) assay, and cellular uptake using inductively coupled plasma optical emission spectroscopy (ICP-OES). Mouse embryonic fibroblasts (NIH-3T3) were selected as a model cell line, due to their susceptibility to the coating-dependent toxicity of AgNPs, and exposed to 40 μg mL^{-1} AgNPs because at this concentration citrate-coated AgNPs are toxic, while AgNPs completely coated with EG_6OH do not affect significantly the cell viability.[20,21] After 24 h of exposure to NPs, as shown in Fig. 3a, the MTT viability assay revealed that the surface coverage significantly determines the toxic activity of the AgNPs; cell viability drastically increases with the increasing EG_6OH density on the surface of AgNPs and, in agreement with what was previously observed,[20] becomes not significantly affected compared to control (ctrl), *i.e.* cells treated with vehicle solution (2 mM sodium citrate), when the saturation density of the ligand on the NP surface is reached. In agreement with the viability results, double fluorescence labeling of actin (red) and nucleus (blue) showed

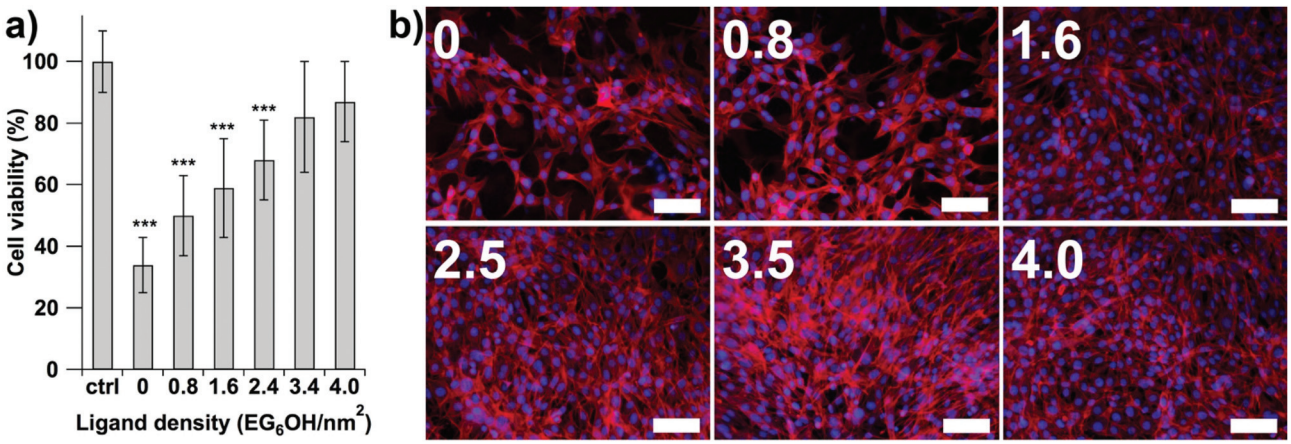

Fig. 3 (a) Cell viability of NIH-3T3 cells after 24 h of treatment with 40 μg mL^{-1} of AgNPs as a functional ligand density. Data are presented as mean ± standard deviation (SD). Statistical analysis was performed using ANOVA followed by Tukey's test. ***$p < 0.001$ denotes significant differences with respect to control (ctrl, cells treated with vehicle solution). (b) Fluorescence micrographs of cells labeled specifically for actin (red) and the nucleus (blue) after 24 h of incubation with 40 μg mL^{-1} AgNPs as a functional ligand density (EG_6OH per nm^2) (scale bar: 100 μm).

surface coating-depending toxicity of AgNPs (see Fig. 3b and Fig S3 in the ESI† for non-merged images). At low EG_6OH density values, cytoskeleton size and density of fibroblasts treated with AgNPs are reduced, thus revealing an impaired ability to replicate and less adhesion to the substrate. The increase of ligand density clearly decreases the toxic effects of AgNPs, in fact, approaching the saturation density; the morphology and density of cells treated with AgNPs are similar to those of cells treated with vehicle solution (control, see the ESI – Fig. S4†). Note that the quantitative analysis of NIH-3T3 nuclei per area showed a trend that is completely in agreement with what was observed above (see Table S5 in the ESI†).

For a deeper understanding of the role of surface coating on the mode of cell death, NIH-3T3 cells were double-stained with acridine orange/ethidium bromide (AO/EB) following 48 h of exposure to AgNPs. Data were extracted from the fluorescence microscopy images based on the percentages of green (viable cells), red (necrotic cells), yellow (early apoptosis), and orange (late apoptosis) fluorescence cells (see Fig. S5 in the ESI† for representative images),[44] and the results are shown in Fig. 4a and summarized in Table S6 in the ESI.† Consistently with the MTT viability assay, the inhibition of cell proliferation after 48 h of exposure to AgNPs shows a trend that is completely in agreement with what was observed at 24 h (Fig. 3a), in fact, the increase of EG_6OH density on the nanoparticle surface drastically reduces their cytotoxic activity, further confirming its key role in the interaction between NPs and cells. Moreover, double-staining assay clearly showed that, independently of the ligand density, AgNPs induce cell death leading mainly to their apoptosis and, to a lesser extent, necrosis. These results are in agreement with what was previously observed.[45–48] Noteworthily, while the percentage of total apoptotic cells is inversely proportional to EG_6OH density, there is no correlation with the percentage of necrotic cells; however, in all cases, necrosis is the least relevant cell death process. From these results, we can infer that, although the surface coverage plays a key role in the extent of cytotoxic activity, the process by which AgNPs mainly induce cell death remains the same independently of the surface coverage of the nanoparticles. Considering that AgNPs carry out their toxic effects after cell internalization,[20,49] these results suggested that EG_6OH density determines the toxic activity of AgNPs by regulating their cellular uptake. In order to probe whether the variation of surface coverage was correlated with the variation of NP internalization, we have assessed the relationship between ligand density and uptake of AgNPs in NIH-3T3 cells by ICP-OES analysis. The cellular uptake was measured following a 6 h incubation with the same concentration of AgNPs functionalized with different EG_6OH densities and extensive washing of NIH-3T3 cells, therefore silver per cell ratios represent AgNPs that were either tightly bound to the cell membrane or actually internalized (see the Experimental section). A shorter incubation time than that used for previous studies was chosen to ensure the nanoparticle uptake, but preventing cell detachment that follows the toxic activity of the nanoparticles. This was confirmed by assessing that the cell number after 6 h of exposure to AgNPs was found to be similar to that of cells treated with vehicle solution (2 mM sodium citrate), regardless of the ligand density. As shown in Fig. 4b, silver uptake drastically decreases with the increasing EG_6OH density, in fact, cells treated with citrate-coated AgNPs (ligand density = 0) show a silver uptake 200 times higher than those treated with nanoparticles completely coated with EG_6OH (ligand density = 4). Noteworthily, this large uptake difference was also qualitatively revealed by the presence of dark spots, due to fluorescence quenching by metal NPs, in the actin

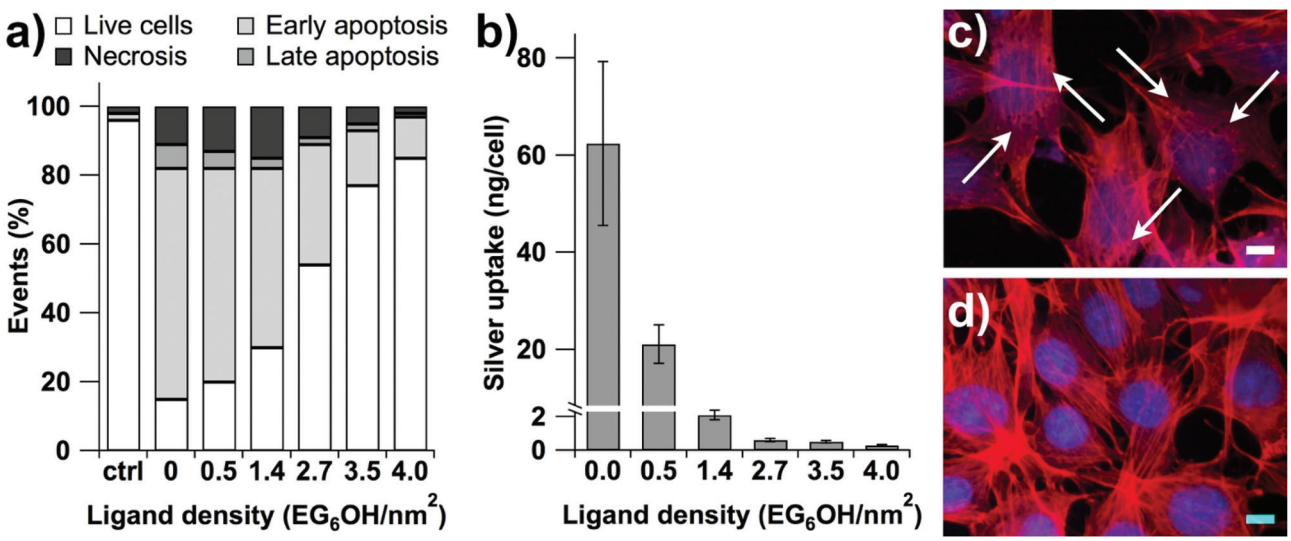

Fig. 4 (a) Double-staining assay of NIH-3T3 cells treated with 40 μg mL^{-1} of AgNPs after 48 h of incubation as a functional ligand density. (b) Silver uptake of NIH-3T3 cells after 6 h of exposure to 40 μg mL^{-1} of AgNPs as a functional ligand density. Data are presented as mean ± SD. Fluorescence micrographs of the NIH-3T3 cells labeled specifically for actin (red) and the nucleus (blue) after 24 h of incubation with 40 μg mL^{-1} of AgNPs with ligand density (c) 0 and (d) 4.0 EG_6OH per nm^2, white arrows identify dark spots due to fluorescence quenching by metal NPs (scale bar: 10 μm).

cytoskeleton image of cells treated with citrate-coated AgNPs (see white arrows in Fig. 4c and Fig S6 in the ESI† for non-merged images), but they are not present in those of cells treated with AgNPs completely coated with EG_6OH (Fig. 4d). Therefore, cellular uptake of NPs, as well as the extent and composition of the protein layer adsorbed on their surface and their cytotoxic activity, is strongly correlated to the degree of ligands replaced on their surface, while they induce cell death mainly by apoptosis, regardless of their surface coverage.

Overall, considering that citrate-coated AgNPs are taken up into the NIH-3T3 cells *via* receptor-mediated endocytosis,[20] our results suggest that the increase of EG_6OH density does not affect the NP uptake pathway, but rather the endocytosis process is gradually inhibited by the following decrease of protein adsorption, regulating their cellular uptake and, in turn, their cytotoxic effect.

Experimental

Materials

Silver nitrate ($AgNO_3$), sodium citrate ($C_6H_5O_7Na_3$), tannic acid ($C_{76}H_{52}O_{46}$), (11-mercaptoundecyl)hexa(ethylene glycol) (EG_6OH), Ellman's reagent, dimethyl sulfoxide (DMSO), 3-(4,5-dimethyl-2-thiazolyl)-2,5-diphenyltetrazolium bromide (MTT), MEM Non Essential Amino Acids (NEAA), Dulbecco's phosphate buffered saline (DPBS) and Dulbecco's modified Eagle's medium (DMEM) were purchased from Sigma-Aldrich and used without further purification. All aqueous solutions were prepared with deionized water obtained using an ultrafiltration system (Milli-Q, Millipore) with a measured resistivity of above 18 MΩ. Fetal bovine serum (FBS) was purchased from Gibco and heat-inactivated before use.

Synthesis of citrate-coated AgNPs

Citrate-stabilized AgNPs were prepared following the method reported elsewhere.[29,50] In brief, 100 mL of an aqueous solution of sodium citrate (5 mM) and tannic acid (0.025 mM) was refluxed and an aqueous solution of silver nitrate (1 mL, 25 mM) was added quickly. Then, the reaction mixture was refluxed for 30 min, resulting in a bright yellow colloidal silver solution, and was then allowed to cool down to room temperature. The aqueous suspension of AgNPs was purified by two rounds of centrifugation (30 000*g* for 2 h) and resuspension in 10 mL of an aqueous solution of sodium citrate (2 mM).

Characterization of AgNPs

UV-Vis-NIR spectra were recorded on a Jasco V-560 UV-Vis spectrophotometer and a Thermo Scientific Varioskan Flash Multimode Reader. Dynamic light scattering (DLS) and zeta potential measurement were performed in phosphate buffer (1 mM, pH = 7) and KCl (1 mM) on a NanoBrook Omni Particle Size Analyser (Brookhaven Instruments Corporation, USA) equipped with a 35 mW red diode laser (nominal 640 nm wavelength). AgNPs were characterized using a Transmission Electron Microscopy (TEM) FEI Tecnai F20 ST, equipped with a CCD Camera Gatan MSC704 and an X-Ray EDS spectrometer EDAX EDS PV9761. TEM samples were prepared by drop casting 5 microliters of nanoparticle solutions onto a carbon-coated copper grid, then blotted with filter paper to remove excess solution and dried in air for 20 min. The average size and size distribution of citrate-stabilized AgNPs were measured using ImageJ software by counting 1000 particles. Silver concentrations were measured using an Inductively Coupled Plasma Optical Emission Spectrometer (ICP-OES) Varian Liberty 200. The concentration of silver was measured by ICP-OES titration at λ_{Ag} = 328.068.

Saturation ligand density

The concentration of AgNPs was measured by combining ICP-OES titration and TEM. The as-prepared water dispersed AgNPs were thoroughly mixed at room temperature overnight with a freshly prepared aqueous solution of EG_6OH (~2 mM) adjusting the added volume to achieve a stoichiometry of ~10 EG_6OH per nm^2 that ensures to exceed the maximum ligand density. Nanoparticle-free control samples containing an equal concentration of EG_6OH were prepared. After incubation, AgNPs were pelleted by centrifugation (13 000*g* for 30 min) and the supernatant containing the excess of thiol molecules was transferred to a new tube. The thiol concentrations both in the supernatant and in a nanoparticle-free control sample were measured with Ellman's reagent[51] and used to calculate the saturation ligand density.

Functionalization of AgNPs

The as-prepared water dispersed AgNPs were thoroughly mixed at room temperature overnight with a freshly prepared aqueous solution of EG_6OH adjusting the thiol concentration to achieve several samples with stoichiometry in the range between 0 EG_6OH per nm^2 and saturation. Nanoparticle-free control samples containing an equal concentration of EG_6OH were prepared. After incubation, AgNPs were purified by four rounds of centrifugation (13 000*g* for 30 min) and resuspension in an aqueous solution of sodium citrate (2 mM). The thiol concentrations of nanoparticle-free control samples were measured with Ellman's reagent[51] and used to calculate the ligand density.

Salt stability of AgNPs

AgNPs were mixed in 1 : 19 volume ratio with aqueous solutions of NaCl in sodium citrate (2 mM).

Ion exchange chromatography

Diethylaminoethyl (DEAE) Sepharose was prepared as specified by the manufacturer and equilibrated in sodium citrate (2 mM). 30 μL of nanoparticles were incubated with 50 mg of resin in a 1.5 mL tube for 1 h on a rotating wheel. The unbound nanoparticles were recovered and successive washes of the resin were then performed using phosphate buffer (10 mM, pH = 7) with an increasing amount of NaCl. The amount of the recovered nanoparticles was quantified by the measurement of absorbance at 400 nm.

Serum protein adsorption

Silver nanoparticles (100 μL) were mixed in 1 : 5 volume ratio with complete medium (DMEM supplemented with 10% (v/v) heat-inactivated FBS, 2 mM L-glutamine, 0.1 mM MEM Non Essential Amino Acids (NEAA), 100 U mL^{-1} of penicillin and 100 U mL^{-1} of streptomycin) and incubated overnight at 37 °C. The nanoparticles were purified by three rounds of centrifugation (22 000*g* for 30 min at 4 °C) and resuspended in 100 μL of an aqueous solution of phosphate buffer (1 mM, pH = 7) and KCl (1 mM).

Polyacrylamide gel electrophoresis (PAGE)

AgNPs (100 μL) were washed by two rounds of centrifugation (13 000*g* for 20 min at 4 °C) and resuspended in 40 μL of Tris-Cl (10 mM, pH 7.4). 8 μl of 6× Laemmli SDS sample reducing buffer (Bio Rad) was added to the nanoparticles and incubated at 100 °C for 5 min to reduce and denature proteins on the surface of the particles. Nanoparticles were removed by centrifugation (13 000*g* for 20 min at 4 °C) and the supernatants containing the free proteins, along with a molecular weight ladder (Bio Rad), were loaded on 10% SDS-PAGE and resolved at 100 V for 60 min. The gel was fixed with a solution of 25% isopropyl alcohol, 10% glacial acetic acid for 60 min and stained with colloidal Coomassie Blue G-250 for 2 h. Gel densitometry was performed using image J software.

Mass spectrometry analysis and protein identification

As reported above, protein separation was performed by PAGE using a 4–20% precast polyacrylamide gel (Bio Rad). The resulting gel was stained overnight with colloidal Coomassie Blue G-250 and seven bands, labeled A–G, were excised for mass spectrometry analysis. Protein digestion was performed following a protocol reported in the literature.[52] Coomassie-stained bands were diced into 1 mm^3 cubes, destained for 30 min with 50% acetonitrile in 100 mM ammonium bicarbonate buffer, dehydrated with 100% acetonitrile for 10 min, reduced with 10 mM DTT (1,4-dithiothreitol, Sigma Aldrich) for 30 min at 56 °C and alkylated with 55 mM iodoacetamide (IAA, Sigma Aldrich) for 30 min in the dark. After alkylation, gel pieces were dehydrated with 100% acetonitrile and digested overnight with MS-grade trypsin (Thermo Fisher, 13 ng μl^{-1} in ammonium bicarbonate buffer 10 nM with 10% acetonitrile) at 37 °C. The digestion products were extracted with a solution of 5% formic acid and acetonitrile 1 : 2 for 15 min at 37 °C in a shaker and were then lyophilized using a SpeedVac Concentrator (Savant). Dry peptides from bands were resuspended in 40 μL of a mixture of water : acetonitrile : formic acid 97 : 3 : 2, sonicated for 10 min at room temperature and centrifuged (12 100*g* for 10 min). Analyses were performed on an ESI† Q Exactive Mass spectrometer (Thermo Scientific) controlled using Xcalibur (v. 29 build 2926) and interfaced with an Ultimate 3000 UHPLC pump. The column (Zorbax SB-C18 RRHT, 2.1 × 50 mm, 1.8 μ particle size, Agilent Technologies) was equilibrated with 0.3 ml min^{-1} of water 0.1% formic acid (A) with 2% acetonitrile (B); after sample injection (18 μl), B% was raised from 2 to3%, then linearly increased from 3 to 21% in 19 min; B% was then brought to 90% in 4 min and kept at 90% B for 3 min before the reconditioning step. The total runtime was 35 min. The ESI source was operated in positive mode; probe was heated at 290 °C, the capillary temperature was set at 270 °C; the following nitrogen flows (arbitrary units) were used to assist the ionization: Sheath Gas 40, Aux Gas 30, Sweep Gas 3; capillary voltage was set to 3.8 kV, the S-Lens RF level was set at 45 (arbitrary units). Profile MS and MS^2 spectra were recorded from 200 to 2000 m/z in FULL MS/dd-MS^2 (TOP5) mode, at a resolution of 70 000 and 17 500, respectively. The five most intense multi-charged ions were selected for MS^2 nitrogen-promoted collision-induced dissociation (NCE = 28). A precursor active exclusion of 20 seconds was set; peptide-like isotope pattern ions were preferred. The mass spectrometer was calibrated before the start of the analyses. Raw data, converted into mascot generic format using MsConvert (v. 3.0.10730, ProteoWizard tools), were searched against Swiss-Prot (accessed Oct 2018; 6002 sequences for *Bos Taurus*) for peptide sequences and C-RAP for contaminants with MASCOT (Version 2.4, Matrix Science, London, UK). Trypsin as proteolytic enzyme and carbamidomethyl cysteine as fixed modification were set in search parameters. Deamidated (NQ) and oxidated (M) were set as variable modifications. One missed cleavage was allowed. Mass tolerances were set at 10 ppm for the precursor ions and 0.05 Da for the product ions. Automatic decoy database search was used to estimate the false discovery rate, which was adjusted to ≤1%.

Cell cultures

Mouse embryonic fibroblast (NIH-3T3) cells were cultured under standard conditions in the DMEM medium supplemented with 10% (v/v) heat-inactivated FBS, 2 mM L-glutamine, 0.1 mM MEM Non Essential Amino Acids (NEAA), 100 U mL^{-1} of penicillin and 100 U mL^{-1} of streptomycin in a humidified incubator set at 37 °C with 5% CO_2. The cells were seeded in 96-well plates at a density 1×10^4 cells per well and grown for 24 h before exposure to nanoparticles.[53] For the control, the cell culture medium was diluted with sodium citrate (2 mM) to ensure that dilution of the medium by the solution of nanoparticles has no impact on the cell performance.

Actin and nucleus staining

The cells were fixed with 4% paraformaldehyde in DPBS, washed with DPBS. They were then permeabilized with 0.001% Triton-X 100. The cells were labelled with TRITC-conjugated phalloidin (FAK100, Merck Millipore) for 1 h, followed by rinses with DPBS. Actin staining was critical to map the local orientation of actin filaments within the cells. Nuclear counterstaining was performed by incubation with DAPI (FAK100, Merck Millipore) for 3 min, followed by rinses with DPBS. The samples were examined using a Nikon Eclipse 80i microscope equipped for fluorescence analysis.

Cell viability (cytotoxicity assay)

Cell viability was determined by 3-(4,5-di-methyl-2-thiazolyl)-2,5-diphenyltetrazolium bromide (MTT) assay, measuring the intracellular reduction of tetrazolium salts into purple formazan by viable cells.[54] Briefly, the cells were seeded in 96-well plates with complete medium with or without nanoparticles for 24 h and 48 h under standard conditions. After incubation times, the medium with or without AgNPs was discarded, and the cells were washed with 100 μL of DPBS and then 100 μL of complete medium was added. Afterwards, 10 μL of sterile MTT solution (5 mg mL^{-1} in DPBS) was added to each well and incubated for 2 h at 37 °C with 5% CO_2. Subsequently, the medium was discarded and 200 μL of DMSO was added to each sample to solubilize formazan crystals. Optical density (OD) was read on a microplate reader (Thermo Scientific Varioskan Flash Multimode Reader) at 550 nm as a working wavelength and 640 nm as a reference. Cell viability was calculated as the proportion of the mean OD of the replicated wells relative to that of the control.

Fluorescence microscopic analysis of cell death

A combination of fluorescent DNA-binding dyes acridine orange (AO) and ethidium bromide (EB) was used to detect the cells' death morphology, according to the standard procedure.[55] The cells were seeded in 24-well plates at a density 4×10^4 cells per well and grown for 24 h before exposure to nanoparticles. After 48 h of exposure, the cells were treated with trypsine-EDTA 1×, neutralized with DPBS and collected by centrifugation. Then, fluorescent dyes AO (1 g L^{-1}) and EB (1 g L^{-1}) were added to the cellular pellet. The cell suspension was dropped on a glass slide and covered by a coverslip. Slides were observed with a Nikon Eclipse 80i fluorescence microscope equipped with a UV-mercury lamp. Percentages of viable, apoptotic and necrotic cells were measured by analyzing 100 cells.

In vitro uptake of AgNPs

The uptake of AgNPs by NIH-3T3 cells was quantified using Inductively Coupled Plasma Optical Emission Spectroscopy (ICP-OES). AgNPs were incubated for 6 h with pre-seeded NIH-3T3 cells in 12-well plates at a density of 1×10^5 cells per well. After exposure, the medium was discarded and the cells were washed three times with DPBS to remove residual NPs. Then, the cells were treated with trypsin-EDTA 1×, neutralized with DPBS, counted and collected by centrifugation. The recovered pellets were treated with 200 μL of lysis buffer (RIPA buffer), digested overnight with freshly prepared aqua regia (HNO_3 : HCl = 1 : 3) and then diluted with 2% HNO_3. The concentration of silver was measured by ICP-OES at 328.068 nm. Operating conditions of the ICP-OES are listed below: RF power, 1200 W; plasma Ar flow rate, 12 L min^{-1}; nebulizer Ar flow rate, 0.70 L min^{-1}; uptake time, 25 s; stabilization time, 15 s. A series of silver standard solutions (20, 10, 5, 2.5, 1.5, 0.5, and 0 ppm) in HNO_3 2% were prepared to obtain a calibration curve used to determine the silver amount taken up by the cells in each sample, and the concentration reported for each sample is the mean value of 5 different measures.

Statistical analysis

All data represented the mean ± standard deviation (SD) of at least 4 independent culture experiments. Statistical significance was determined using a one-way analysis of variance with Tukey's test for multiple comparisons using Origin 8 software (OriginLab Corporation). Differences were considered significant when $p < 0.005$ and $p < 0.001$.

Conclusions

In the present study, we have shown the role of surface coverage of nanoparticles in serum protein adsorption, cellular uptake and cytotoxicity. The surface properties of AgNPs were modulated through the controlled displacement of citrate ions with an oligo(ethylene glycol)-based ligand; the ligand density has been varied between no ligand (only citrate ions) and saturation. The exposure to serum-containing media revealed that the extent and composition of the serum proteins layer adsorbed on the AgNPs, *i.e.* protein corona, is strongly dependent on the EG_6OH density. The protein resistance of AgNPs increases following the increase of EG_6OH density; however, the adsorption of proteins was not completely eliminated even at the saturation density. Although BSA was the most abundant protein detected in the corona, our results suggest that ApoE is the one whose amount is most affected by the ligand density. The different extent and composition of protein corona on the AgNPs significantly determine their cellular uptake and cytotoxicity, in fact, both silver uptake and toxic activity drastically decrease with the increasing EG_6OH density. However, the surface coating has no effect on the process by which AgNPs mainly induce cell death that, in fact, occurs mainly through apoptosis regardless of ligand density. We can infer that the drastically different biological outcomes of AgNPs as a function of their surface coverage can be ascribed to the different ability to adsorb serum proteins which, in turn, regulate the toxic activity of AgNPs regulating their cellular uptake *via* receptor-mediated endocytosis.

In summary, our results reveal that the synergism between the surface coverage and biological identity of NPs can be exploited for their rational design and engineering, thus thoroughly tailoring the interaction of NPs with living systems to specific applications and minimizing the side effects.

Conflicts of interest

There are no conflicts to declare.

Acknowledgements

The authors thank the Fondazione Cassa di Risparmio di Modena for funding the UHPLC-ESI-Q Exactive system at the

Centro Interdipartimentale Grandi Strumenti (CIGS). M. B. was supported by the project MIUR-PRIN prot. 2017YH9MRK.

References

1 G. Y. Chen, I. Roy, C. H. Yang and P. N. Prasad, *Chem. Rev.*, 2016, **116**, 2826–2885.
2 L. Cheng, C. Wang, L. Feng, K. Yang and Z. Liu, *Chem. Rev.*, 2014, **114**, 10869–10939.
3 J. A. Barreto, W. O'Malley, M. Kubeil, B. Graham, H. Stephan and L. Spiccia, *Adv. Mater.*, 2011, **23**, H18–H40.
4 E.-K. Lim, T. Kim, S. Paik, S. Haam, Y.-M. Huh and K. Lee, *Chem. Rev.*, 2015, **115**, 327–394.
5 M. Rahman, S. Laurent, N. Tawil, L. H. Yahia and M. Mahmoudi, *Protein-Nanoparticle Interactions: The Bio-Nano Interface*, Springer Berlin Heidelberg, 2013.
6 Editorial, *Nat. Nanotechnol.*, 2019, **14**, 1083–1083.
7 S. Wilhelm, A. J. Tavares, Q. Dai, S. Ohta, J. Audet, H. F. Dvorak and W. C. W. Chan, *Nat. Rev. Mater.*, 2016, **1**, 16014.
8 Q. Dai, S. Wilhelm, D. Ding, A. M. Syed, S. Sindhwani, Y. Zhang, Y. Y. Chen, P. MacMillan and W. C. W. Chan, *ACS Nano*, 2018, **12**, 8423–8435.
9 C. D. Walkey and W. C. W. Chan, *Chem. Soc. Rev.*, 2012, **41**, 2780–2799.
10 M. P. Monopoli, F. B. Bombelli and K. A. Dawson, *Nat. Nanotechnol.*, 2011, **6**, 11–12.
11 T. Cedervall, I. Lynch, S. Lindman, T. Berggård, E. Thulin, H. Nilsson, K. A. Dawson and S. Linse, *Proc. Natl. Acad. Sci. U. S. A.*, 2007, **104**, 2050.
12 R. Lima, A. B. Seabra and N. Durán, *J. Appl. Toxicol.*, 2012, **32**, 867–879.
13 J. Skalska and L. Strużyńska, *Folia Neuropathol.*, 2015, **53**, 281–300.
14 R. B. Foldbjerg and H. Autrup, *Arch. Basic Appl. Med.*, 2013, **1**, 5–15.
15 M. E. Samberg and N. A. Monteiro-Riviere, in *Encyclopedia of Nanotechnology*, ed. B. Bhushan, Springer Netherlands, Dordrecht, 2012, pp. 1069–1077.
16 N. Durán, G. Nakazato and A. B. Seabra, *Appl. Microbiol. Biotechnol.*, 2016, **100**, 6555–6570.
17 P. Aggarwal, J. B. Hall, C. B. McLeland, M. A. Dobrovolskaia and S. E. McNeil, *Adv. Drug Delivery Rev.*, 2009, **61**, 428–437.
18 N. Liu, M. Tang and J. Ding, *Chemosphere*, 2020, **245**, 125624.
19 M. E. Vance, T. Kuiken, E. P. Vejerano, S. P. McGinnis, M. F. Hochella Jr., D. Rejeski and M. S. Hull, *Beilstein J. Nanotechnol.*, 2015, **6**, 1769–1780.
20 M. Barbalinardo, F. Caicci, M. Cavallini and D. Gentili, *Small*, 2018, **14**, 1801219.
21 F. Decataldo, M. Barbalinardo, D. Gentili, M. Tessarolo, M. Calienni, M. Cavallini and B. Fraboni, *Adv. Biosyst.*, 2020, **4**, 1900204.
22 P. Harder, M. Grunze, R. Dahint, G. M. Whitesides and P. E. Laibinis, *J. Phys. Chem. B*, 1998, **102**, 426–436.
23 S. Herrwerth, W. Eck, S. Reinhardt and M. Grunze, *J. Am. Chem. Soc.*, 2003, **125**, 9359–9366.
24 L. Y. Li, S. F. Chen, J. Zheng, B. D. Ratner and S. Y. Jiang, *J. Phys. Chem. B*, 2005, **109**, 2934–2941.
25 D. Gentili, P. D'Angelo, F. Militano, R. Mazzei, T. Poerio, M. Brucale, G. Tarabella, S. Bonetti, S. L. Marasso, M. Cocuzza, L. Giorno, S. Iannotta and M. Cavallini, *J. Mater. Chem. B*, 2018, **6**, 5400–5406.
26 K. L. Prime and G. M. Whitesides, *Science*, 1991, **252**, 1164–1167.
27 K. L. Prime and G. M. Whitesides, *J. Am. Chem. Soc.*, 1993, **115**, 10714–10721.
28 L. Duchesne, D. Gentili, M. Comes-Franchini and D. G. Fernig, *Langmuir*, 2008, **24**, 13572–13580.
29 N. G. Bastus, F. Merkoci, J. Piella and V. Puntes, *Chem. Mater.*, 2014, **26**, 2836–2846.
30 J. C. Love, L. A. Estroff, J. K. Kriebel, R. G. Nuzzo and G. M. Whitesides, *Chem. Rev.*, 2005, **105**, 1103–1170.
31 H. Hinterwirth, S. Kappel, T. Waitz, T. Prohaska, W. Lindner and M. Lämmerhofer, *ACS Nano*, 2013, **7**, 1129–1136.
32 M. D. Torelli, R. A. Putans, Y. Tan, S. E. Lohse, C. J. Murphy and R. J. Hamers, *ACS Appl. Mater. Interfaces*, 2015, **7**, 1720–1725.
33 D. Gentili, G. Ori, L. Ortolani, V. Morandi and M. Cavallini, *ChemNanoMat*, 2017, **3**, 874–878.
34 H. Chen, X. Kou, Z. Yang, W. Ni and J. Wang, *Langmuir*, 2008, **24**, 5233–5237.
35 Y. Ishihama, Y. Oda, T. Tabata, T. Sato, T. Nagasu, J. Rappsilber and M. Mann, *Mol. Cell. Proteomics*, 2005, **4**, 1265–1272.
36 L. D. Unsworth, H. Sheardown and J. L. Brash, *Langmuir*, 2008, **24**, 1924–1929.
37 C. D. Walkey, J. B. Olsen, H. Guo, A. Emili and W. C. Chan, *J. Am. Chem. Soc.*, 2012, **134**, 2139–2147.
38 S. Wagner, A. Zensi, S. L. Wien, S. E. Tschickardt, W. Maier, T. Vogel, F. Worek, C. U. Pietrzik, J. Kreuter and H. von Briesen, *PLoS One*, 2012, **7**, e32568.
39 A. L. Barran-Berdon, D. Pozzi, G. Caracciolo, A. L. Capriotti, G. Caruso, C. Cavaliere, A. Riccioli, S. Palchetti and A. Lagana, *Langmuir*, 2013, **29**, 6485–6494.
40 H. Gao and Q. He, *Expert Opin. Drug Delivery*, 2014, **11**, 409–420.
41 V. H. Nguyen, N. M. Meghani, H. H. Amin, T. T. D. Tran, P. H. L. Tran, C. Park and B. J. Lee, *Colloids Surf., B*, 2018, **170**, 179–186.
42 Y. Yan, K. T. Gause, M. M. Kamphuis, C. S. Ang, N. M. O'Brien-Simpson, J. C. Lenzo, E. C. Reynolds, E. C. Nice and F. Caruso, *ACS Nano*, 2013, **7**, 10960–10970.
43 A. Akinc, W. Querbes, S. De, J. Qin, M. Frank-Kamenetsky, K. N. Jayaprakash, M. Jayaraman, K. G. Rajeev, W. L. Cantley, J. R. Dorkin, J. S. Butler, L. Qin, T. Racie, A. Sprague, E. Fava, A. Zeigerer, M. J. Hope, M. Zerial, D. W. Sah, K. Fitzgerald, M. A. Tracy, M. Manoharan, V. Koteliansky, A. Fougerolles and M. A. Maier, *Mol. Ther.*, 2010, **18**, 1357–1364.

44 K. Liu, P.-c. Liu, R. Liu and X. Wu, *Med. Sci. Monit. Basic Res.*, 2015, **21**, 15–20.
45 P. V. AshaRani, G. Low Kah Mun, M. P. Hande and S. Valiyaveettil, *ACS Nano*, 2009, **3**, 279–290.
46 N. Miura and Y. Shinohara, *Biochem. Biophys. Res. Commun.*, 2009, **390**, 733–737.
47 Y.-H. Lee, F.-Y. Cheng, H.-W. Chiu, J.-C. Tsai, C.-Y. Fang, C.-W. Chen and Y.-J. Wang, *Biomaterials*, 2014, **35**, 4706–4715.
48 Y.-H. Hsin, C.-F. Chen, S. Huang, T.-S. Shih, P.-S. Lai and P. J. Chueh, *Toxicol. Lett.*, 2008, **179**, 130–139.
49 E. Caballero-Díaz, C. Pfeiffer, L. Kastl, P. Rivera-Gil, B. Simonet, M. Valcárcel, J. Jiménez-Lamana, F. Laborda and W. J. Parak, *Part. Part. Syst. Charact.*, 2013, **30**, 1079–1085.
50 J. Hühn, C. Carrillo-Carrion, M. G. Soliman, C. Pfeiffer, D. Valdeperez, A. Masood, I. Chakraborty, L. Zhu, M. Gallego, Z. Yue, M. Carril, N. Feliu, A. Escudero, A. M. Alkilany, B. Pelaz, P. del Pino and W. J. Parak, *Chem. Mater.*, 2016, **29**, 399–461.
51 C. K. Riener, G. Kada and H. J. Gruber, *Anal. Bioanal. Chem.*, 2002, **373**, 266–276.
52 A. Shevchenko, H. Tomas, J. Havli, J. V. Olsen and M. Mann, *Nat. Protoc.*, 2007, **1**, 2856.
53 M. Barbalinardo, D. Gentili, F. Lazzarotto, F. Valle, M. Brucale, M. Melucci, L. Favaretto, M. Zambianchi, A. I. Borrachero-Conejo, E. Saracino, V. Benfenati, D. Natalini, P. Greco, M. G. Di Carlo, G. Foschi and M. Cavallini, *Small Methods*, 2018, **2**, 1700377.
54 P. R. Twentyman and M. Luscombe, *Br. J. Cancer*, 1987, **56**, 279–285.
55 M. K. Squier and J. J. Cohen, *Mol. Biotechnol.*, 2001, **19**, 305–312.